One-Pot Synthesis of Liquid Hg/Solid β-HgS Metal–Semiconductor Heterostructures with Unique Electrical Properties

Lei Wu,[†,‡] Baogang Quan,[†] Yaling Liu,[†,*] Rui Song,[‡,*] and Zhiyong Tang[†,*]

[†]Laboratory for Nanomaterials, National Center for Nanoscience and Technology, Beijing 100190, P. R. China and [‡]College of Chemistry and Chemical Engineering, Graduate University of Chinese Academy of Sciences, Beijing 100049, P. R. China.

ABSTRACT Liquid metal–solid semiconductor heterostructures, Hg heads combined with single-crystalline β-HgS tails, with controllable sizes and well-defined interfaces have been fabricated for the first time *via* one-pot synthesis. Such heterostructures can exist in water with good stability due to coordination adsorption of cysteine molecules onto the surface of both Hg and HgS through Hg–S bonds. Two-probe current–voltage curve measurements reveal that good ohmic contacts without additional resistance contacts are generated at the interfaces of Hg/β-HgS heterostructures. Only existence of ohmic contacts offers many potential applications of metal–semiconductor heterostructures in minimization of electronic devices.

KEYWORDS: heterostructures · metal · semiconductor · one-pot synthesis · coordination · ohmic contact

Nano/microscale metal–semiconductor heterostructures have attracted many scientific and industrial interests due to their potential applications in modern electrical devices.[1−13] As an example, one-dimensional (1D) semiconductor nanorods or nanowires are believed to become good candidates for the next generation of electrical elements, such as field-effect transistors (FETs), because of their small sizes and good electrical performances. To integrate such semiconductor nanorods or nanowires into the circuit, good electrical contact between them is needed, which can be implemented by a connection with metal particles.[4−13] Encouraged by this prospect, different types of 1D heterostructures with metal heads and semiconductor tails, *e.g.,* Au/CdSe,[13] Pt/CdS,[14] Ag/CdSe,[15] and Au/Te,[16] have been successfully prepared. However, before applying the 1D heterostructures in the electrical devices, a big challenge should be overcome: The solid–-solid interfaces between metal and semiconductor still give rise to considerable contact resistance that impedes charge transport among semiconductor nanorods or nanowires.[17]

A suggested strategy is to replace solid metal heads in the heterostructures with liquid Hg. Despite the potential toxicity in environment and biology, Hg has exhibited some unique and irreplaceable characteristics in nano/microscale devices. Previous studies confirmed that liquid Hg could work as good junctions or excellent test beds for molecular electronics through its advantages of easy assembly, high versatility, and freedom from structural features (no edges, steps, terraces, or dislocations that result in defects) over the conventional solid metals such as Au, Ag, and Pt.[18] So, fabrication and application of Hg-based liquid–solid heterostructures with good ohmic contacts in electronics not only can solve the problem of contact resistance faced in minimization of integrated devices but also can provide a new candidate for study of charge transport in the device and device arrays with various structures. However, until now there is no report on the preparation and property of Hg-based heterostructures, which might originate from the difficulty in their synthesis. In general, the conventional preparation methods of heterostructures involve two individual steps: Metal heads or semiconductor tails are first synthesized and subsequently transferred to the other mother solution for growth of the complementary parts. However, the two-step techniques seem not suitable for obtaining Hg-based heterostructures, because the switching between different solutions will greatly increase the amounts of Hg waste products and, more importantly, during synthesis small-sized liquid Hg particles will easily merge into large Hg drops driven by minimization of their surface tension. Therefore a novel preparation strategy is highly desirable.

* Address correspondence to zytang@nanoctr.cn, liuyl@nanoctr.cn, rong@gucas.ac.cn.

Received for review December 15, 2010 and accepted February 8, 2011.

Published online February 18, 2011
10.1021/nn103473s

Herein we report one-pot synthesis of 1D Hg/β-HgS liquid metal−solid semiconductor heterostructures. Cysteine (H_2SR, R = $-CH_2CH(NH_2)COO^-$) is one of the typical amino acids with three functional groups (−SH, −COOH, and $-NH_2$) and exists widely in organisms, and it has been explored as one of the key factors to cause biotoxic effects because of the strong affinity of thiol groups of cysteine to heavy metal ions such as Hg^{2+}.[19−30] Furthermore, cysteine is an unstable compound and is easily oxidized or decomposed by metal ions especially in alkaline solution.[30] For instance, reactions between Hg^{2+} and cysteine possibly give rise to products of either elementary Hg or binary HgS by altering the experimental conditions.[31−35] Followed by the above bioprocess, it is very interesting to construct Hg/HgS heterostructures through one step by directly mixing Hg^{2+} and cysteine in alkaline aqueous solution, if the synthesis conditions are carefully controlled. Using this method, we successfully prepare 1D Hg/β-HgS metal−semiconductor heterostructures for the first time *via* one-pot synthesis. Moreover, such heterostructures exhibit the unique electrical properties that are definitely attractive for development of nano/microscale devices.

RESULTS AND DISCUSSION

Morphology and Structure of Hg/β-HgS Heterostructures. One-pot synthesis method is used to prepare 1D Hg/β-HgS liquid metal−solid semiconductor heterostructures by directly mixing Hg^{2+} and cysteine in alkaline aqueous solution. Similar to Ag(I)/cysteine system that we previously reported,[36,37] the growth of Hg/β-HgS heterostructures are also susceptible to the reaction conditions, such as precursor molar ratio, pH value of the reprepared reaction system, and reaction temperature. Only when the molar ratio of Hg^{2+} and cysteine is fixed at 1:1 and the pH value of the system is adjusted to 11.70 are the pure heterostructure products (Figure 1a−c) obtained after 9 days at a constant temperature of 23 °C (see details in Methods). It is worth noting that the heterostructures can be obtained at a rather wide reaction temperature ranging from 23 to 45 °C. Higher temperature benefits the rapid growth of the heterostructures but is against the controllable shapes of the products (Figure S1 in the Supporting Information). Seen from the magnified scanning electron microscopy (SEM) images in Figure 1b,c, it is obvious that all the formed 1D nanomaterials are composed of one round head and one tail with a sharp end. Moreover, the sizes of the products are uniform, and the interface between the head and the tail for each heterostructure is well-defined.

To investigate the components and structure of the heterostructures, a series of characterizations were done. First, energy-dispersive X-ray (EDX) elemental analysis and mapping were used to make clear the elemental distribution in different parts of the heterostructures. Figure 1d and 1e show the corresponding results of *in situ* selected-area EDX elemental analysis of the head and tail, respectively. It is obvious that the atomic ratio of Hg and S in the head is different from that in the tail. In the head, the content of Hg is much higher than S (the ratio of Hg to S is about 6:1, Table S1 in the Supporting Information), but to the tail, the atomic ratio of Hg and S is nearly 1:1 (Table S1 in the Supporting Information), indicating that the components in the head and tail are distinctly different from each other for such heterostructures. The result of EDX elemental mapping (Figure S2 in the Supporting Information) is consistent with that of EDX elemental analysis, confirming that the content of Hg in the head is higher than that in the tail.

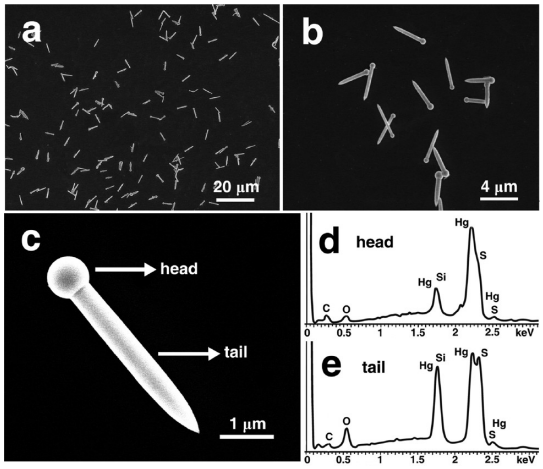

Figure 1. (a, b) SEM images of the products obtained at 23 °C and dispersed on the surface of Si substrate; (c) high-magnified SEM image of an individual heterostructure; (d, e) *in situ* selected-area EDX spectra of the head and the tail of the produced heterostructure, respectively.

The heterostructures shown in Figure 1a−c were analyzed in detail by powder X-ray diffraction (XRD), differential scanning calorimetry (DSC), and transmission electron microscopy (TEM). Figure 2 demonstrates the powder XRD patterns of such heterostructures measured at room temperature (bottom) and −75 °C (top). The XRD data at room temperature (the bottom pattern) can be assigned to the crystalline β-HgS, suggesting that β-HgS is one component of the heterostructures.[38] Moreover, while the measured temperature is decreased to −75 °C (the melting or crystalline point of Hg is −38.5 °C), five new peaks appear in the XRD pattern (the top pattern), which are well indexed to the lattice planes (101), (003), (110), (104), and (113) of hexagonal crystalline Hg, respectively. No peak assigned to other impurities is detected, revealing that the heterostructures are made up of two components: Liquid Hg and solid β-HgS. Both DSC and TEM results further confirm the existence of these two components in the heterostructures. Figure 3 shows the DSC thermogram of the heterostructures. During the temperature-rising period from −55 °C back to room temperature after the cooling process, an endothermal peak appears at the temperature of about −38.32 °C, which is perfectly matched with the melting point of Hg (−38.5 °C), clearly indicating that liquid metal Hg is one

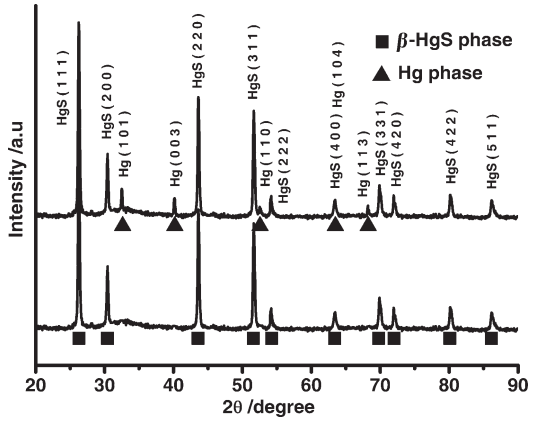

Figure 2. Powder XRD patterns of the heterostructures measured at room temperature (bottom pattern) and −75 °C (top pattern), respectively.

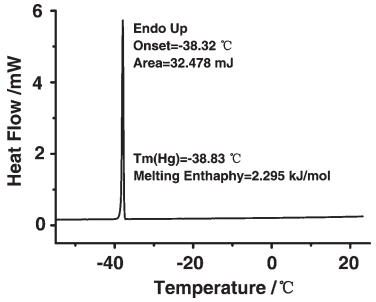

Figure 3. DSC thermogram of the heterostructures.

part of the heterostructures. Finally, the exact location of Hg and HgS in 1D heterostructures was explored by selected-area electron diffraction (SAED) pattern and high-resolution TEM (HRTEM) image (Figure 4). A typical TEM image is shown in Figure 4a, and the corresponding SAED pattern and HRTEM image of the part marked by an arrow in Figure 4a are illustrated in Figure 4b and 4c,d, respectively. The SAED pattern is consistent with that of β-HgS incident from [011] axis, and no changes of the SAED pattern are observed in different sections of the tail. Moreover, as seen from Figure 4d, the spacing about 0.335 nm between two adjacent lattice planes is close to the spacing of (111) planes (0.339 nm) in the crystal of β-HgS. Altogether, both of these results are indexed with the unit cell of β-HgS, revealing that the tail of the heterostructure is single crystalline β-HgS and its growth direction is along the [111] direction. Since the tail is assigned to HgS, the head of the heterostructure should be liquid Hg, which is also proved by TEM survey since no well-defined electron diffraction pattern (not shown) is obtained on the head part due to the amorphous nature of liquid Hg.

Interestingly, such heterostructures with liquid Hg heads and solid β-HgS tails can exist stably in water for at least 1 year. It is curious why Hg heads in liquid state do not merge with each other to minimize their surface tension. A plausible explanation is that the thiol groups of cysteine in solution bind with Hg and β-HgS to form Hg−S−C coordination bonds owing to their high

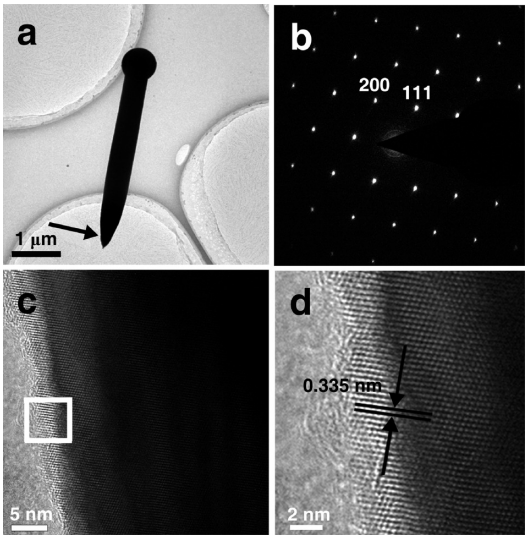

Figure 4. (a) TEM image of an individual heterostructure; (b) corresponding SAED pattern of the tail; (c) HRTEM image of the part marked by an arrow in panel a; (d) magnified HRTEM image of the part labeled in panel c.

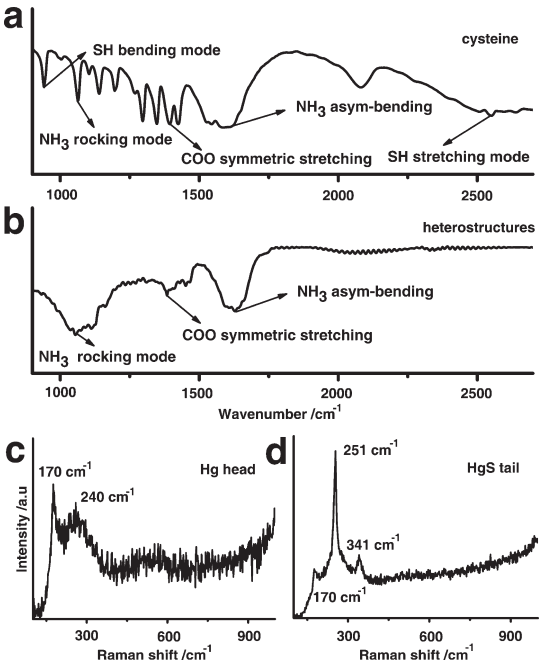

Figure 5. FT-IR spectra performed by using pressed pellets of a mixture of KBr with (a) cysteine or (b) heterostructures; (c, d) Micro-Raman spectra of the Hg head and the β-HgS tail, respectively.

affinity for metal Hg and Hg^{2+},[39] which prevents not only the merging of Hg heads but also the volatilization of Hg.[35] Figure 5 panels a and b show the Fourier transform infrared spectroscopy (FT-IR) spectra of free cysteine molecules and heterostructures, respectively. Compared with these two spectra, it is obvious that both spectra exhibit the characteristic bands at 1063 cm^{-1} attributed to the $-NH_3$ rocking mode, 1603 cm^{-1} assigned to the $-NH_3$ asymmetric bending mode, and 1380 cm^{-1} assigned to the symmetric

stretching of $-COO^-$. However, the peaks at 939 and 2540 cm^{-1}, respectively, attributed to $-SH$ bending and stretching mode totally vanish in the spectra of heterostructures,[40,41] indicating formation of strong Hg−S−C coordination bonds between cysteine and the heterostructures, namely, on the surface of the heterostructures. That is the reason why the element S can be detected in the head of the heterostructures in the characterization results of EDX elemental analysis and EDX elemental mapping (Figure 1c and Figure S2 in the Supporting Information).

The micro-Raman spectra further confirm the existence of Hg−S−C bonds on the surface of both liquid Hg heads and β-HgS tails in the heterostructures. Figure 5 panels c and d represent the micro-Raman spectra observed on Hg head and β-HgS tail of single Hg/β-HgS heterostructure, respectively. For the head (Figure 5c), both the sharp peak at about 170 cm^{-1} and the broad peak at about 240 cm^{-1} are attributed to the δ(C−S−Hg) skeletal bending mode.[42] Similarly, the peak at about 170 cm^{-1} observed on the β-HgS tail (Figure 5d) is also assigned to the skeletal bending mode of δ(C−S−Hg), which is obviously distinguished from the peaks originating from the vibration of the Hg−S bonds in the compound of β-HgS (at 251 and 341 cm^{-1}).[43,44]

Growth Mechanism of Hg/β-HgS Heterostructures. Why does a simple mixture of Hg^{2+} and cysteine in alkaline aqueous solution lead to production of the Hg/β-HgS heterostructures, and how does the evolution process occur? Looking over the existing data about cysteine, one can know that alkaline environment benefits oxidization of cysteine to cystine by metal ions,[31] and meanwhile cysteine often functions as sulfur sources or morphology-directing agents in the synthesis processes of metal sulfides.[45,46] In the reaction system of Hg^{2+} and cysteine at pH value of 11.70, cysteine not only works as the reducing agent and the sulfur source for formation of the Hg/β-HgS heterostructures, but also as the capping agent to make the heterostructures stabilized. The reaction procedures can be described by the following set of chemical equations (eqs):

$$RS^-(aq) + \frac{1}{2}Hg^{2+}(aq) \rightarrow \frac{1}{2}Hg^0 + \frac{1}{2}RSSR(aq) \quad (1)$$

$$nHg^0 \rightarrow Hg\ nanospheres(l) \quad (2)$$

$$RS^-(aq) + OH^-(aq) \rightarrow \frac{1}{2}O_2(g) + RH(aq) + S^{2-}(aq) \quad (3)$$

$$Hg^{2+}(aq) + S^{2-}(aq) \rightarrow HgS(s, black) \quad (4)$$

where RS^- and RSSR represent cysteine ion and cystine ion, respectively; aq is the abbreviation of aqueous, demonstrating that all the ions exist in aqueous solution; l, s, and g are the abbreviation of liquid, solid, and gas, respectively, describing the existing state of the products in each chemical reaction.

Adopted from the data in the textbooks and references,[47−49] the changes of Gibbs energy for every chemical reaction in the reaction procedure are estimated as follows (see part S2 in the Supporting Information): −64.45 kJ·mol^{-1} for eq 1, 0 kJ·mol^{-1} for eq 2, 127.74 kJ·mol^{-1} for eq 3, and −297.90 kJ·mol^{-1} for eq 4. The difference in Gibbs energy of four equations determines the reaction direction and order. For example, the changes of Gibbs energies for formation of liquid Hg nanospheres (NSs, eq 1 + 2) and HgS (eq 3 + 4) are estimated to be −64.45 and −170.16 kJ·mol^{-1}, respectively (see part S2 in the Supporting Information), indicating that both Hg NSs and β-HgS are spontaneously produced in this reaction system. Moreover, greater energy is needed to overcome the occurrence of chemical reaction (3) compared with reaction (1) (the products of both RSSR and RH are detected by ESI-MS, Figure S3 in the Supporting Information), suggesting that the formation of Hg NSs is prior to that of HgS. So, in this reaction system, the chemical reaction occurs one by one according to the reaction procedures proposed above. First, the oxidation−reduction reaction between Hg^{2+} and cysteine occurs (eq 1), and then Hg^0 products tend to aggregate with each other and gradually evolve into liquid Hg NSs (eq 2). Subsequently, the S^{2-} is released slowly *via* reaction 3, and meanwhile β-HgS begins to generate and deposit on the surface of Hg NSs (eq 4) to finally form the 1D Hg/β-HgS heterostructures.

The investigation on the intermediate states at different reaction times experimentally confirms the growth mechanism proposed above. Figure 6a−d shows the morphological evolution of the products as the reaction time extends. At the beginning of the growth process, liquid Hg NSs (Figure 6a) are formed first. After 48 h of reaction, β-HgS begins to generate and grow on the surface of Hg NS (Figure 6b). In general, an exact 1D structure is formed originating from a single droplet, which follows a typical liquid−solid growth mechanism,[50] so a β-HgS tail with a sharp end is formed on the surface of every Hg NS herein. Moreover, the longer the reaction time is, the longer the tail is (Figure 6b−d). The statistic data of the diameters of Hg heads and the lengths of β-HgS tails *versus* the reaction time are shown in Figure 6e (also in Figure S4 and S5 in the Supporting Information). It is obvious that the growth rate of Hg heads is much slower than that of β-HgS tails as the reaction time exceeds 48 h, indicating that the formation of β-HgS tails is slow but dominating after 48 h of reaction in the system. This observation is consistent with the suggested reaction procedures, in which the Gibbs energy change for the formation of final HgS products is large (−170.16 kJ·mol^{-1} for eq 3 + 4 *vs* −64.45 kJ·mol^{-1} for eq 1 + 2) but is energy-unfavorable for intermediate products (127.74 kJ·mol^{-1} for eq 3 *vs* −64.45 kJ·mol^{-1} for eq 1).

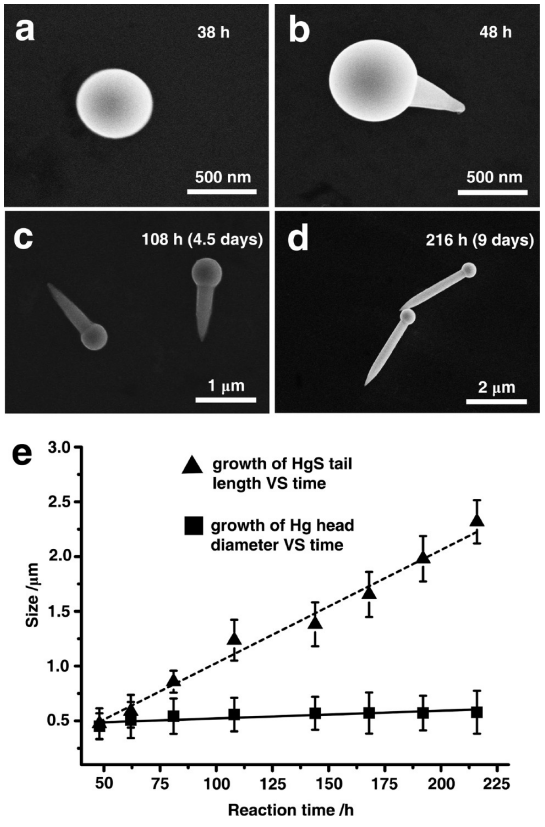

Figure 6. (a−d) Morphological evolution of the products at 23 °C as the reaction lengthens: (a) Hg spheres formed after 38 h; (b−d) Hg/β-HgS heterostructures formed after (b) 48, (c) 108, and (d) 216 h. (e) Statistic data of the diameters of Hg heads and the lengths of β-HgS tails *versus* the reaction time.

Electrical Properties of Hg/β-HgS Heterostructures. The nature of the heterointerface determines the properties of the heterostructure device, and 1D metal-semiconductor heterostructures with only ohmic current−voltage (I−V) characteristics are important to nano/microdevices because of their necessity in interconnection and packing among all the multicomponent nanosystems.[17] To evaluate the electrical properties of Hg/β-HgS heterostructures and understand the contact characteristic of Hg/β-HgS interface, devices based on the heterostructures are fabricated on the reprepared Au/Ti electrode gap arrays (Figure S6 in the Supporting Information), and two-probe I−V curves are measured.

Two types of devices (one type based on an individual Hg/β-HgS heterostructure as shown in the inset of Figure 7a, and the other only based on β-HgS tail as shown in the inset of Figure 7b) are constructed through adjusting the deposition positions of Pt nanowires using the electron beam assisted deposition technique. The corresponding I−V characteristics for these two devices are investigated using a Lakeshore vacuum probe station equipped with a liquid nitrogen cryostat and a Keithley 4200 SCS, and the typical results are plotted in Figure 7 panels a and b, respectively. Similar symmetrical and linear I−V characteristics are observed for all the devices, demonstrating that ohmic contacts are formed

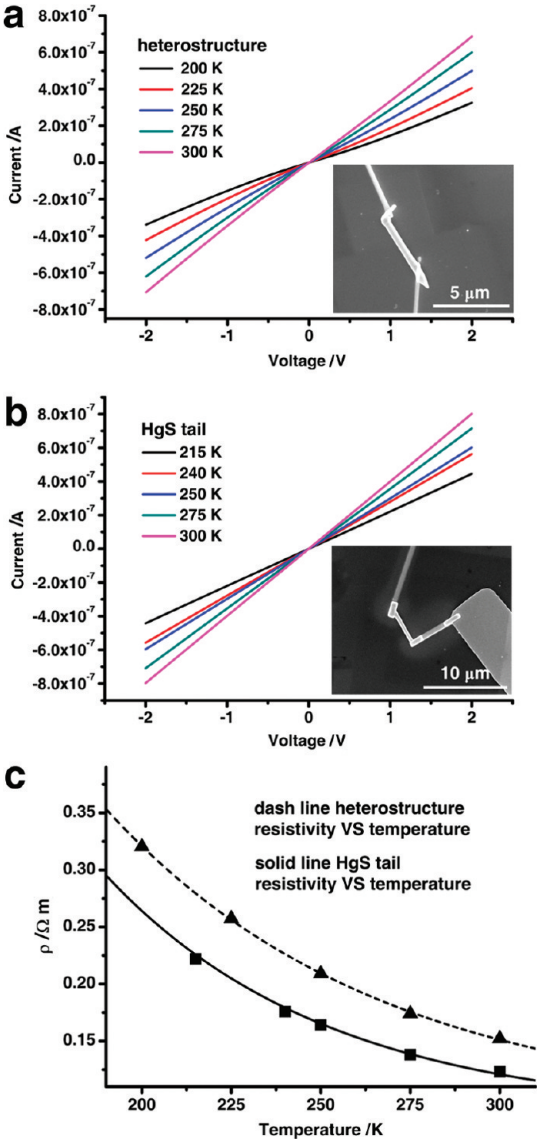

Figure 7. Two-probe I−V curves of the devices based on (a) an individual Hg/β-HgS heterostructure and (b) β-HgS tail at various temperatures. Insets are the corresponding device images monitored by SEM. (c) Corresponding ρ−T plots of the devices. The data are average values from at least 10 individual measurements.

between the Hg head and the β-HgS tail in every heterostructure.[17,51] Moreover, as the temperature decreases from 300 to 200 K, namely, while the state of the Hg head is changed from liquid to solid (the morphology of the heterostructure remains the same as the temperature decreases, Figure S7 in the Supporting Information), identical I−V characteristics are always observed, and the current at a certain voltage gradually decreases. Figure 7c shows the corresponding resistivity−temperature (ρ−T) plots for these devices. Whether the device is fabricated based on the heterostructure or only on the β-HgS tail, ρ exhibits exponential decay *versus* T, suggesting that both devices based on the heterostructure and β-HgS tail exhibit similar semiconductor behaviors. The semiconductor feature of β-HgS is also observed from the

absorption spectrum of the heterostructures, and the band gap of β-HgS tails is estimated to be 0.28 eV (Figure S8 in the Supporting Information). From the $I-V$ results, we can deduce that β-HgS is a semiconductor material and the Hg head acts as electrodes in the heterostructures, and importantly good ohmic contacts are formed at the heterointerface of every Hg/β-HgS heterostructure. The unique electrical properties make such Hg/β-HgS heterostructures attractive for study of nanoscale electrical transport as well as development of new types of nanodevices.

In summary, we constructed Hg/β-HgS metal-semiconductor heterostructures *via* one-pot synthesis. Such heterostructures are combined by liquid Hg heads and single-crystalline β-HgS tails, and are stably dispersed in water due to strong adsorption of cysteine molecules onto the surface of both Hg heads and β-HgS tails. Two-probe $I-V$ curve measurements reveal that good ohmic contacts are formed at the interfaces of Hg/β-HgS nanostructures. The advantages of adjustable sizes, good stability, and unique electrical properties make the fabricated Hg/β-HgS heterostructures attractive for study of nanoscale electrical transport as well as development of new types of nanodevices. Moreover, the protective molecules with various functional groups (*i.e.*, cysteine stabilizers contain both $-$COOH and $-NH_2$ groups) surrounding the heterostructures can be expected to be used as linkers to integrate functional arrays in devices or conjugate with biomolecules in sensors.

METHODS

Synthesis of Hg/β-HgS Heterostructures. All chemicals used were of analytical grade or the highest purity available, and 18 MΩ·cm deionized water refined by Millipore-Q Academic system was used as solvent. The reaction system was prepared in a vial first by dissolving 0.01 M cysteine and 0.01 M $Hg(ClO_4)_2 \cdot 3H_2O$ in deionized water under vigorous stirring with final pH value of around 11.70 (adjusted by 2 M NaOH carefully). Then, the vial was transferred immediately into an oven with a constant and fixed temperature (any temperature from 23 to 45 °C). Black precipitates were produced after several days. Subsequently, the products were centrifuged and washed with additional deionized water for several times to remove unreacted precursors and salts.

Characterization of Hg/β-HgS Heterostructures. The products were characterized by scanning electron microscopy (SEM, Hitachi S-4800), energy-dispersive X-ray spectra (EDX, Horiba EMAX 7593-H), differential scanning calorimetry (DSC, PerkinElmer Diamond), transmission electron microscopy (TEM, Tecnai G^2 F20 U-TWIN), X-ray diffraction (XRD, Panalytical X'Pert-Pro MPD), Fourier transform infrared spectroscopy (FT-IR, PE2000), micro-Raman spectroscopy (Renishaw inVia), and electrospray ionization mass spectrum (ESI−MS, LC/MS-2010), from which the morphology, structure, and growth mechanism of Hg/β-HgS heterostructures could be observed and elucidated.

Device Fabrication and Electrical Measurements of Hg/β-HgS Heterostructures. The devices based on the heterostructures were fabricated by the following procedures. First, the prepared heterostructures were dispersed onto SiO_2/Si wafers (the thickness of the SiO_2 layer was about 500 nm) with Au/Ti electrode gap arrays prefabricated by photolithography. Then, Pt nanowires were deposited on each side of one heterostructure to make it connected with adjacent Au/Ti electrodes by electron beam assisted deposition in a Nova 200 Nanolab SEM/FIB DualBeam system. A 5 KeV electron beam was used during the deposition process. Two-probe current−voltage ($I-V$) characterizations of the heterostructures were carried out with a Lakeshore vacuum probe station equipped with a liquid nitrogen cryostat and recorded using a Keithley 4200 SCS.

Acknowledgment. The authors are grateful to Wenping Hu (Institute of Chemistry, Chinese Academy of Sciences) for providing $I-V$ measuring equipments, and acknowledge financial support from the National Natural Science Foundation for Distinguished Youth Scholars of China (21025310, Z.Y.T.), National Natural Science Foundation of China (20901019, Y.L.L.; 20973047, Z.Y.T.; 91027011, Z.Y.T.), National Research Fund for Fundamental Key Project (2009CB930401, Z.Y.T.), China−Korea Joint Research Project (2010DFA51700, Z.Y.T.), and 100-Talent Program of Chinese Academy of Sciences (Z.Y.T.).

Supporting Information Available: Additional experimental data, including SEM images of the products at 37 °C, EDX data of head and tail, EDX mapping results, ESI-MS result of the intermediate products, statistic data of the diameter of Hg head and the length and the diameter of β-HgS tail, SEM images of the reprepared Au/Ti electrode gap arrays, cryo-EM image of the heterostructures, absorption spectra and corresponding plots of $(\alpha h\nu)^{1/2}$ *vs* $h\nu$ for indirect transitions, and estimation of Gibbs energy changes in the reaction procedure. This material is available free of charge *via* the Internet at http://pubs.acs.org.

REFERENCES AND NOTES

1. Milliron, D. J.; Hughes, S. M.; Cui, Y.; Manna, L.; Li, J. B.; Wang, L. W.; Alivisatos, A. P. Colloidal Nanocrystal Heterostructures with Linear and Branched Topology. *Nature* **2004,** *430*, 190–195.
2. Yin, Y. D.; Alivisatos, A. P. Colloidal Nanocrystal Synthesis and the Organic−Inorganic Interface. *Nature* **2005,** *437*, 664–670.
3. Carbone, L.; Cozzoli, P. D. Colloidal Heterostructured Nanocrystals: Synthesis and Growth Mechanisms. *Nano Today* **2010,** *5*, 449–493.
4. Mokari, T.; Sztrum, C. G.; Salant, A.; Rabani, E.; Banin, U. Formation of Asymmetric One-Sided Metal-Tipped Semiconductor Nanocrystal Dots and Rods. *Nat. Mater.* **2005,** *4*, 855–863.
5. Steiner, D.; Mokari, T.; Banin, U.; Millo, O. Electronic Structure of Metal−Semiconductor Nanojunctions in Gold CdSe Nanodumbbells. *Phys. Rev. Lett.* **2005,** *95*, 056805–056808.
6. Salant, A.; Amitay-Sadovsky, E.; Banin, U. Directed Self Assembly of Gold-Tipped Semiconductor Nanorods. *J. Am. Chem. Soc.* **2006,** *128*, 10006–10007.
7. Elmalem, E.; Saunders, A. E.; Costi, R.; Salant, A.; Banin, U. Growth of Photocatalytic CdSe−Pt Nanorods and Nanonets. *Adv. Mater.* **2008,** *20*, 4312–4317.
8. Costi, R.; Saunders, A. E.; Elmalem, E.; Salant, A.; Banin, U. Visible Light-Induced Charge Retention and Photocatalysis with Hybrid CdSe−Au Nanodumbbells. *Nano Lett.* **2008,** *8*, 637–641.
9. Maynadié, J.; Salant, A.; Falqui, A.; Respaud, M.; Shaviv, E.; Banin, U.; Soulantica, K.; Chaudret, B. Cobalt Growth in the Tips of CdSe Nanorods. *Angew. Chem., Int. Ed.* **2009,** *48*, 1814–1817.
10. Menagen, G.; Macdonald, J. E.; Shemesh, Y.; Popov, I.; Banin, U. Au Growth on Semiconductor Nanorods: Photoinduced *versus* Thermal Growth Mechanisms. *J. Am. Chem. Soc.* **2009,** *131*, 17406–17411.
11. Costi, R.; Cohen, G.; Salant, A.; Rabani, E.; Banin, U. Electrostatic Force Microscopy Study of Single Au−CdSe Hybrid

Nanodumbbells: Evidence for Light-Induced Charge Separation. *Nano Lett.* **2009,** *9*, 2031–2039.
12. Shaviv, E.; Banin, U. Synergistic Effects on Second Harmonic Generation of Hybrid CdSe−Au Nanoparticles. *ACS Nano* **2010,** *4*, 1529–1538.
13. Mokari, T.; Rothenberg, E.; Popov, I.; Costi, R.; Banin, U. Selective Growth of Metal Tips onto Semiconductor Quantum Rods and Tetrapods. *Science* **2004,** *304*, 1787–1790.
14. Habas, S. E.; Yang, P. D.; Mokari, T. Selective Growth of Metal and Binary Metal Tips on CdS Nanorods. *J. Am. Chem. Soc.* **2008,** *130*, 3294–3295.
15. Chakrabortty, S.; Yang, J. A.; Tan, Y. M.; Mishra, N.; Chan, Y. Asymmetric Dumbbells from Selective Deposition of Metals on Seeded Semiconductor Nanorods. *Angew. Chem., Int. Ed.* **2010,** *49*, 2888–2892.
16. Lin, Z. H.; Lin, Y. W.; Lee, K. H.; Chang, H. T. Selective Growth of Gold Nanoparticles onto Tellurium Nanowires *via* a Green Chemical Route. *J. Mater. Chem.* **2008,** *18*, 2569–2572.
17. Agarwal, R. Heterointerfaces in Semiconductor Nanowires. *Small* **2008,** *4*, 1872–1893.
18. Rampi, M. A.; Whitesides, G. M. A Versatile Experimental Approach for Understanding Electron Transport Through Organic Materials. *Chem. Phys.* **2002,** *281*, 373–391.
19. Moreau, J. W.; Weber, P. K.; Martin, M. C.; Gilbert, B.; Hutcheon, I. D.; Banfield, J. F. Extracellular Proteins Limit the Dispersal of Biogenic Nanoparticles. *Science* **2007,** *316*, 1600–1603.
20. Meldrum, F. C.; Cölfen, H. Controlling Mineral Morphologies and Structures in Biological and Synthetic Systems. *Chem. Rev.* **2008,** *108*, 4332–4432.
21. Xu, A. W.; Ma, Y. R.; Cölfen, H. Biomimetic Mineralization. *J. Mater. Chem.* **2007,** *17*, 415–449.
22. Yu, S. H.; Cölfen, H. Bio-inspired Crystal Morphogenesis by Hydrophilic Polymers. *J. Mater. Chem.* **2004,** *14*, 2124–2147.
23. Garnweitner, G.; Niederberger, M. Organic Chemistry in Inorganic Nanomaterials Synthesis. *J. Mater. Chem.* **2008,** *18*, 1171–1182.
24. Cölfen, H.; Yu, S. H. Biomimetic Mineralization/Synthesis of Mesoscale Order in Hybrid Inorganic−Organic Materials *via* Nanoparticle Self-Assembly. *MRS Bull.* **2005,** *30*, 727–735.
25. Yu, S. H. Bioinspired Crystal Growth by Synthetic Templates. *Top. Curr. Chem.* **2007,** *271*, 79–118.
26. Harrison, M. T.; Kershaw, S. V.; Burt, M. G.; Rogach, A.; Eychmüller, A.; Weller, H. Investigation of Factors Affecting the Photoluminescence of Colloidally-Prepared HgTe Nanocrystals. *J. Mater. Chem.* **1999,** *9*, 2721–2723.
27. Taylor, N. J.; Carty, A. J. Nature of Mercury(2+) Ion L-cysteine Complexes Implicated in Mercury Biochemistry. *J. Am. Chem. Soc.* **1977,** *99*, 6143–6145.
28. Jalilehvand, F.; Leung, B. O.; Izadifard, M.; Damian, E. Mercury(II) Cysteine Complexes in Alkaline Aqueous Solution. *Inorg. Chem.* **2006,** *45*, 66–73.
29. Matzapetakis, M.; Ghosh, D.; Weng, T. C.; Penner-Hahn, J. E.; Pecoraro, V. L. Peptidic Models for the Binding of Pb(II), Bi(III) and Cd(II) to Mononuclear Thiolate Binding Sites. *J. Biol. Inorg. Chem.* **2006,** *11*, 876–890.
30. Hoffmeyer, R. E.; Singh, S. P.; Doonan, C. J.; Ross, A. R. S.; Hughes, R. J.; Pickering, I. J.; George, G. N. Molecular Mimicry in Mercury Toxicology. *Chem. Res. Toxicol.* **2006,** *19*, 753–759.
31. Giles, N. M.; Watts, A. B.; Giles, G. I.; Fry, F. H.; Littlechild, J. A.; Jacob, C. Metal and Redox Modulation of Cysteine Protein Function. *Chem. Biol.* **2003,** *10*, 677–693.
32. Song, F. Y.; Briseno, A. L.; Zhou, F. M. Redox Reactions of and Transformation between Cysteine-Mercury Thiolate and Cystine in Metallothioneins Adsorbed at a Thin Mercury Film Electrode. *Langmuir* **2001,** *17*, 4081–4089.
33. Maret, W.; Vallee, B. L. Thiolate Ligands in Metallothionein Confer Redox Activity on Zinc Clusters. *Proc. Natl. Acad. Sci. U.S.A.* **1998,** *95*, 3478–3482.
34. Jiang, L. J.; Maret, W.; Vallee, B. L. The Glutathione Redox Couple Modulates Zinc Transfer from Metallothionein to Zinc-Depleted Sorbitol Dehydrogenase. *Proc. Natl. Acad. Sci. U.S.A.* **1998,** *95*, 3483–3488.
35. Anderson, D. L. Use of L-cysteine for Minimization of Inorganic Hg Loss during Thermal Neutron Irradiation. *J. Radioanal. Nucl. Chem.* **2009,** *282*, 11–14.
36. Li, C.; Deng, K.; Tang, Z. Y.; Jiang, L. Twisted Metal-Amino Acid Nanobelts: Chirality Transcription from Molecules to Frameworks. *J. Am. Chem. Soc.* **2010,** *132*, 8202–8209.
37. Li, C.; Tang, Z. Y.; Jiang, L. Easy Patterning of Silver Nanoparticle Superstructures on Silicon Surfaces. *J. Mater. Chem.* **2010,** *20*, 9608–9612.
38. Hao, A. M.; Gao, C. X.; Li, M.; He, C. Y.; Huang, X. W.; Zhang, D. M.; Yu, C. L.; Liu, H. W.; Ma, Y. Z.; Tian, Y. J.; Zou, G. T. A Study of the Electrical Properties of HgS under High Pressure. *J. Phys.: Condens. Matter* **2007,** *19*, 425222–425230.
39. Love, J. C.; Estroff, L. A.; Kriebel, J. K.; Nuzzo, R. G.; Whitesides, G. M. Self-Assembled Monolayers of Thiolates on Metals as a Form of Nanotechnology. *Chem. Rev.* **2005,** *105*, 1103–1169.
40. Pawlukojć, A.; Leciejewicz, J.; Ramirez-Cuesta, A. J.; Nowicka-Scheibe, J. L-Cysteine: Neutron Spectroscopy, Raman, IR, and *ab Initio* Study. *Spectrochim. Acta Part A* **2005,** *61*, 2474–2481.
41. Shindo, H.; Brown, T. L. Infrared Spectra of Complexes of L-Cysteine and Related Compounds with Zinc(II), Cadmium(II), Mercury(II), and Lead(II). *J. Am. Chem. Soc.* **1965,** *87*, 1904–1909.
42. Hoffmann, G. G.; Brockner, W.; Sternfatt, I. Bis(*n*-alkanethiolato)mercury(II) Compounds, $Hg(SC_nH_{2n+1})_2$ (n = 1−10, 12): Preparation Methods, Vibrational Spectra, GC/MS Investigations, and Exchange Reactions with Diorganyl Disulfides. *Inorg. Chem.* **2001,** *40*, 977–985.
43. Patel, B. K.; Rath, S.; Sarangi, S. N.; Sahu, S. N. HgS Nanoparticles: Structure and Optical Properties. *Appl. Phys. A: Mater. Sci. Process.* **2007,** *86*, 447–450.
44. Hector, A. L.; Henshaw, G.; Parkin, I. P.; Shaw, G. A. Room Temperature Synthesis in Liquid Ammonia of Zinc, Cadmium, and Mercury Sulfides. *Main Group Chem.* **1996,** *1*, 183–187.
45. Zhang, B.; Ye, X. C.; Dai, W.; Hou, W. Y.; Xie, Y. Biomolecule-Assisted Synthesis and Electrochemical Hydrogen Storage of Porous Spongelike Ni_3S_2 Nanostructures Grown Directly on Nickel Foils. *Chem.—Eur. J.* **2006,** *12*, 2337–2342.
46. Zuo, F.; Zhang, B.; Zhao, Y.; Xie, Y. L-Cysteine-Assisted Synthesis of PbS Nanocube-Based Pagoda-like Hierarchical Architectures. *J. Phys. Chem. C* **2008,** *112*, 2831–2835.
47. Atkins, P.; de Paula, J. *Atkins' Physical Chemistry*, 8th ed.; Oxford Press: Oxford, 2006; pp 998−1000.
48. Roux, M. V.; Foces-Foces, C.; Notario, R.; Ribeiro da Silva, M. A. V.; Ribeiro da Silva, M. D. D. M. C.; Santos, A. F. L. O. M.; Juaristi, E. Experimental and Computational Thermochemical Study of Sulfur-Containing Amino Acids: L-Cysteine, L-Cystine, and L-Cysteine-Derived Radicals. S−S, S−H, and C−S Bond Dissociation Enthalpies. *J. Phys. Chem. B* **2010,** *114*, 10530–10540.
49. Dean, J. A. *Lange's Handbook of Chemistry*, 15th ed.; MacGraw-Hill: New York, 1999; pp 6.4−6.6.
50. Kirmse, H.; Häusler, I.; Kret, S.; Janik, E.; Karczewski, G.; Wojtowicz, T. TEM Analysis of the Container Effect of Au-Based Catalyst Droplets during Vapour−Liquid−Solid Growth of Axial ZnTe/CdTe Nanowires. *Crys. Res. Technol.* **2009,** *44*, 1047–1053.
51. Chueh, Y. L.; Ford, A. C.; Ho, J. C.; Jacobson, Z. A.; Fan, Z. Y.; Chen, C. Y.; Chou, L. J.; Javey, A. Formation and Characterization of Ni_xInAs/InAs Nanowire Heterostructures by Solid Source Reaction. *Nano Lett.* **2008,** *8*, 4528–4533.